Image-Based Mechanical Analysis of Multifilamentary Microstructure Formation in Al–Fe Heavily Deformed *In-Situ* Composites

Hiroyuki Toda*, Hiroto Mizutani, Toshiro Kobayashi, Toshikazu Akahori and Mitsuo Niinomi

Department of Production Systems Engineering, Toyohashi University of Technology, Toyohashi, Aichi 441-8580, Japan

It has been reported that nano-scale multifilamentary microstructure, which has been readily available in Al–Nb systems, was hardly realized in Al–Fe heavily-deformed composites systems. In the present study, state-of-the-art techniques are applied to gain basic insight into the necessary requirement for the texture development of the Al–Fe composites. Three-dimensional finite element meshes were generated to monitor local stress and strain distributions in real materials. The approach taken in this study may be characterized as new type of the reverse engineering which is based on the visualization of microstructural features of materials. It has been clarified that local stress elevation occurs where the Fe phase is constricted or gnarled with flection when cutting chips are used as a matrix. Hydrostatic stress varies significantly in the Fe phase thereby promoting the plasticity of the Fe phase. Both sufficient strengthening of aluminum and irregular distribution of the embedded Fe phase are identified essential for multifilamentary microstructure formation.

1. Introduction

Cast and deformed microcomposites such as Cu–Nb, Cu–Ag, and Cu–Cr systems have been reported as ultrahigh-strength materials, which exhibit an anomalous increase in tensile strength with heavy deformation. For example, deformation-processed Cu–Nb alloys have been found to be capable of achieving tensile strengths above 2 GPa.[1] The strain during the deformation process is defined as $\eta = \ln(A_0/A_f)$, where A_0 is the cross-sectional area before deformation and A_f is that after deformation. For these types of composites, the remarkable strengthening is attributed to the BCC phase developing a ribbon-like cross section. The *in-situ* composites exhibit a strength-filament spacing relationship similar to that often observed in cold-worked steel based on pearlite.[2] suggesting that the remarkably high strengthening of Cu-based *in-situ* composites may result from the effect of the BCC metal filaments with respect to the motion of dislocations in the Cu matrix. Considering the mechanisms of both layered-structure formation and strengthening in these Cu-based systems, it can be readily supposed that an analogous procedure might be applicable to other FCC metal-based systems such as aluminum matrix composites.

In fact, Thieme *et al.*, and Toda and Kobayashi, have reported that Al–Nb heavily deformed *in-situ* composites demonstrate superior strength and electrical conductivity[3–5] coupled with reasonable thermal stability.[6] Such heavy deformation was accomplished by swaging in the authors' study. The authors have examined property-microstructure relationships encompassing a Hall–Petch plot of strength vs. filament spacing. It was clarified that there is a linear relationship up to $\eta = 12.4$, while the plot at a higher applied strain deviated from the line. The deviation may be attributed to several possible mechanisms such as transition of the deformation mechanism to a single dislocation motion with bowing between closely spaced planes.[7] However, for linear pileups in a two-phase material, which are predominant up to

a relatively high strain level in the Al–Nb system, it has been reported that the slope in the Hall–Petch type relationship is primarily related to the shear moduli of the two phases.[8,9] This is because the effectiveness of the second phase as planar barriers to dislocation motion in the major phase is related to the modulus of the second phase. Therefore, further strengthening of such metal/metal multifilamentary composites may be possible by incorporating a second phase having a higher shear modulus than that of Nb. From such a point of view, Cr, Fe, Ta, Mo, and W can be identified as ideal candidates for the second phase of the metal/metal multifilamentary composites. Among these, considering the brittle-ductile transition temperature, material cost, and scarcity of resources, Fe may provide a unique possibility to realize the practical usage of such composites.

According to preliminary studies on the production of Al–Fe multifilamentary composites by the present authors,[6] in spite of exhaustive trials, the size of Fe particles (initially around 100 μm in diameter) did not change significantly with an increase in applied strain, η. In these studies, a number of factors related to the matrix, second phase, and processing were varied to determine whether there is a factor that influences the ability to enforce co-deformation of the embedded Fe phase. The factors include diameter, purity and production process of both aluminum and iron particles, matrix hardness, which was varied by either applying the ball milling for different time or chemical composition, and process temperature during swaging. The details of the trials are summarized in Table 1. The typical shape and size of the Fe phase in these Al–Fe composites are shown in Fig. 1 together with those in a nano-scale Al–Nb multifilamentary composite,[4] demonstrating that the Fe particles remain almost intact even after the aluminum matrix has been heavily deformed. Recently, however, some of the present authors have found that the formation of a multifilamentary microstructure is achieved when 5 to 10 vol% of Fe particles are added to aluminum cutting chips in a study in which aluminum cutting chips were consolidated by heavy deformation at room temperature for upgrade recycling.[10,11]

*Corresponding author, E-mail: toda@pse.tut.ac.jp

Table 1 Process variables and their values for Al–Fe heavily deformed *in-situ* composites which have been tried in the preliminary investigation.[6)]

	Process variables tried	Condition	Formation of layered structure
Matrix (Al)	Diameter	3, 5, 45, 50, 177, 400, 840 μm	×
	Purity	2N, 2N5, 3N, 3N7, 4N	×
	Ball milling time	1, 3, 4, 8 h	×
	Chemical composition	Pure Al, Al–Mg–Si alloy	×
	Production procedure	Gas atomizing, chip	◎ (chip)
Second phase (Fe)	Diameter	3, 5, 45, 50, 177, 400, 840 μm	×
	Purity	2N, 2N5, 3N, 3N7, 4N	×
	Production procedure	Reduction, PREP, Carbonyl process, Electrolytic process	×
Process	Temperature	77 K, RT, 473 K	×

(a) Al-Nb

(b) Al-Fe
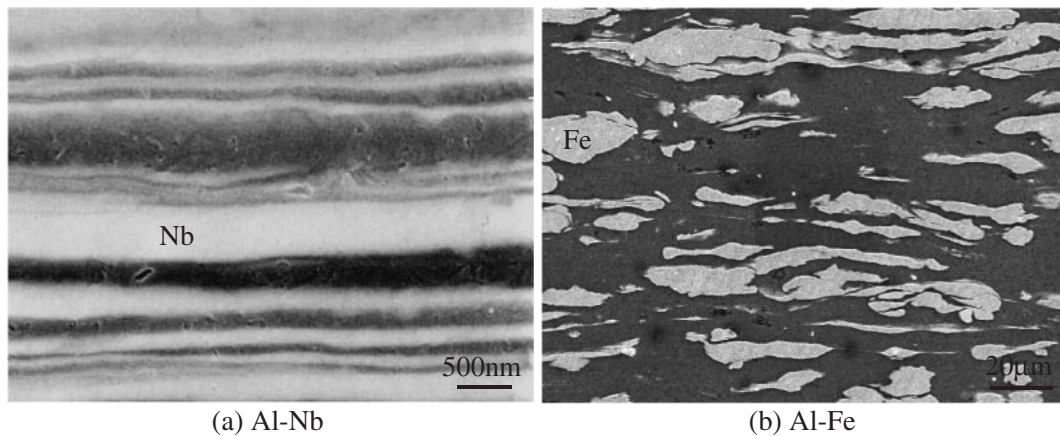
Fig. 1 SEM micrographs of longitudinal cross-sections of Al–Nb and Al–Fe heavily deformed *in-situ* composites.

Despite the unsuccessful results of the exhaustive trials on Al–Fe composites, this clearly implies the existence of a certain processing condition that enables production of Al–Fe multifilamentary composites. Possible processing parameters might be the irregular shape, size, or deformed microstructure of the cutting chip.

In the present study, an attempt was made to gain basic insight into the requirements for the microstructural development of Al–Fe composites. To understand the contribution of the significantly inhomogeneous spatial distribution pattern of the Fe phase in the consolidated cutting chip, which has not been considered in the current literature, three-dimensional visualization of the internal microstructure is clearly valuable. Such three-dimensional information is difficult to obtain by conventional cross-sectional observations, whereas it would appear that X-ray tomography provides a unique possibility. As is well known, advances in tomography have led to the evolution of a new field of manufacturing. This emerging field encompasses reverse engineering techniques where a CAD model of an existing part is created and its performance is modelled with candidate replacement materials. In addition, recent advances in high-resolution imaging have made it possible to readily visualize the microstructural features of materials.[12,13)]

In the present study, three-dimensional finite-element meshes were generated to monitor local stress and strain distributions in real materials. Three Al–Fe composites were produced as model materials using Al–Mg–Si chip, Al powder and Al–Mg–Si powder as their matrices. After the internal microstructures of the Al–Fe composites were visualized, the volume tomographic data sets were converted into stereolithography tessellation language (STL) models to create three-dimensional models for finite-element simulation. Calculated local stress/strain distributions in the Al–Fe composites during the heavy plastic deformation were provided to consider mechanical requirement for the elongation of the Fe phase, together with the results of material tests. Overall, the approach taken in this study may be characterized as a new type of reverse engineering that is based on visualization of the microstructural features of materials.[14,15)]

2. Determination of Analytical Models

2.1 Procedure
2.1.1 Material production

Fe and Al powders having mean diameters of 45 and 28 μm, respectively were used. Purities of the Al and Fe

powders were 99.98 and 99.9%, respectively. The material made from these powders are called Al powder/Fe. In the production of another sample, the cutting chip of a 6061-T651 aluminum alloy was used instead of the pure aluminum powder. The chip was produced by a milling machine in a laboratory at cutting depth of 0.1 mm and cutting speed of 16.7 mm/s. Typical size of the chip was 10 mm in length, 1.2 mm in width and 0.22 mm in thickness. The material made from the aluminum cutting chip and the Fe powder was called Al–Mg–Si chip/Fe hereinafter. The powders were mixed using a V-type mixer for 5.4 ks with rotation frequency of 42 rpm. Volume fraction of the Fe phase is 20%. The mixed powders were uni-axially pressed under a pressure of 118 MPa in room temperature air using a pressing machine having a capacity of 500 kN. The powder compacts were about 20 mm both in diameter and length at this stage. The powder compacts were then filled in a 21.6 mm-o.d. Cu tube, and both ends were roughly sealed by a couple of short Cu cylinders. The billets were then swaged to 1.5 mm in diameter and the Cu skins were removed by etching in HNO_3. Apparent drawing strain including the annihilation of pores reaches 5.4 at this stage. Samples having six different levels of drawing strain were prepared for microstructural observation.

2.1.2 Tomographic imaging and volume rendering

The sample size for tomographic observation was 2 mm maximum diameter. High-resolution X-ray tomography was performed using a laboratory scale computed tomography apparatus (Skyscan Model 1072). Visible light converted from X-rays by a Gd_2O_2S:Tb evaporated film (25 μm in thickness) was captured by a 1024×1024 element two-dimensional cooled CCD detector. A tungsten X-ray tube was used at 98 kV and 100 μA with an apparent X-ray source of 7 μm. A sample was set approximately 74 mm from the X-ray source and 166 mm behind the detector. An aluminum plate of 1 mm in thickness was inserted between the sample and the source to prevent artifacts by the beam hardening effect.[16] A 2×2 mm area of the sample was entirely captured on the CCD camera. A total of 780 radiographs, scanning 180 degrees, were taken along the loading axis at 0.23-degree increments. Each view required 5.9 seconds to acquire the image. Two images were captured at an identical angle and an average image between them was used for reconstruction. Image slices were then reconstructed from the series of projections based on the Feldkamp cone-beam algorithm.[17] The grey-scale value in each dataset was calibrated so that the variation between the most opaque and transparent voxels could be expressed within an 8-bit grey-scale range between 0 and 255. An isotropic voxel with a 2.0 μm edge was achieved in the reconstructed slices. Note that so-called resolution is different from the voxel size. Low contrast resolution of the tomographic set-up should be theoretically more or less worse than the above-mentioned spot size (7 μm).

First, the feature of interest (aluminum matrix in this case) was selected on a two-dimensional reconstructed slice, and a three-dimensional 'seed' growth technique[18,19] was applied to identify the volume of the feature. All voxels that were three-dimensionally connected to the manually set seed point and had a voxel grey value within the set tolerance range

were thresholded and labelled as one feature. The three-dimensional images were rendered by applying ray tracing iso-surface extraction to visualize the surface using front and side diffuse light sources to highlight the three-dimensional character.

2.2 Assessment of deformation behaviours of Fe phase during swaging

As mentioned in the introduction, the deformation of an embedded Fe phase using aluminum powder has not been reported in the available experimental literature, while the formation of a multifilamentary microstructure was achieved when a cutting chip was used for the matrix. This was readily observable in the series of tomographic volumes where the orientations of coarse cutting chips gradually changed before η reached 1.8, with alignment completed in the swaging direction at around $\eta = 1.8$. It has been clarified that the aspect ratio of the Fe phase begins to increase at around $\eta = 1.8$ and subsequently increases from 3.5 to 39.8 at η values between 1.8 and 5.4 in the case of Al–Mg–Si chip/Fe, while such significant elongation is not observed in Al powder/Fe shown in Fig. 2. The tendency of Vickers hardness variations of the Fe phase showed excellent agreement with the volume-based image analyses. For example, the hardness began to increase at around $\eta = 1.8$ and exhibited a significant increase from HV128 to HV213 at η values between 1.8 and 2.7 in Al–Mg–Si chip/Fe, while it increased at most up to HV154 in Al powder/Fe. Strain hardening of the aluminum phase was not observed in either of the materials.

It is interesting to analyse the internal local stress and strain states that cause such phenomenological differences at the specific applied strain range (*i.e.* $\eta = 1.8$). Thus, the first swaging pass after η reached 1.8 (*i.e.* $\eta = 1.8$–2.1) was assumed for model construction in the following numerical analyses.
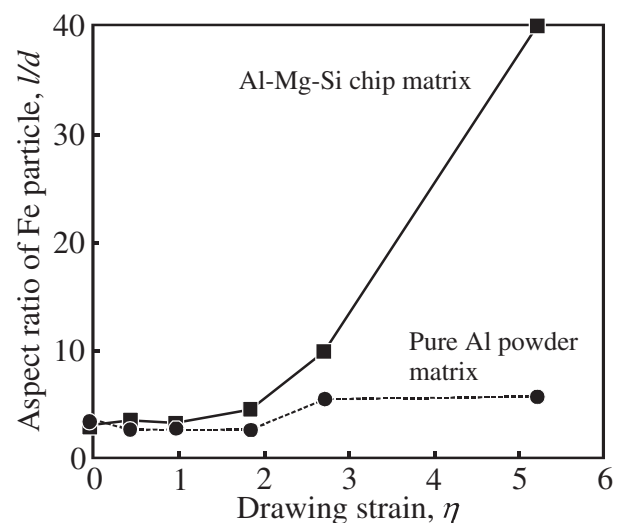

Fig. 2 Variations of aspect ratio of the Fe phase as a function of drawing strain. Two kinds of matrices are shown here.

3. Finite-Element Simulation

3.1 Procedure

3.1.1 Mesh generation from tomographic data

Polygonal models were extracted from the tomographic volumes by tracing iso-grey-value surfaces. Vertex positions of the resulting polygonal mesh were determined by a trilinear interpolation of the surrounding voxel grey values. The extracted models consisted of a very large number of surface triangles at this stage. An appropriate closed bounding box was created by which the polygonal model was bordered with the volume fraction of the embedded Fe phase adjusted to a target volume fraction of 20%. The polygonal models were first exported as an STL file, which was then used for mesh generation for the finite-element analysis using the NASTRAN commercial software package for format conversion. Figure 3 illustrates how microstructure models were created from the whole tomographic volume for the two materials analysed. Since the spatial distribution of the Fe particles was extremely inhomogeneous and the unit size was

much larger in Al–Mg–Si chip/Fe than in Al powder/Fe, the region of interest selected for Al–Mg–Si chip/Fe was approximately 384 times larger in volume than that for Al powder/Fe, as shown in Fig. 3. The matrix aluminum and embedded iron phases were assumed to be linear elastic, followed by work hardening plastically with a perfectly bonded interface in between.

Although only a limited volume extracted from the whole tomographic volume was analysed in this study, as will be described later, reflecting the detailed surface shape in meshing for the finite-element simulation was physically impossible due to the enormous quantity of data involved. Therefore, the number of voxels taken into account during the polygonal surface extraction process was reduced by taking every third voxel into account in Al powder/Fe, thereby reducing the model data size to 1/27. In the case of Al–Mg–Si chip/Fe, every 11th voxel was taken into account, thereby reducing the size to 1/1331. Since the size of the two microstructure models was different, the total mesh numbers became closer by this operation without sacrificing accuracy. To achieve a further drastic reduction in model size, the finite-element analysis was performed in two steps: a small region consisting of both the aluminum and iron phases, which was nested at the centre of a work being swaged, was analysed after the displacement distribution of the work had been analysed in advance. The former is called the 'Microstructure Model' hereafter and was produced reflecting the actual distribution of the Fe phase faithfully by the above-mentioned image-based procedure. The latter is called the 'Swaging Model' and was analysed assuming a mechanically isotropic continuum medium with homogenized material characteristics.

The boundary conditions for the Microstructure Model were set as forced displacements at all of its surface nodes, referring to the corresponding nodal solutions for the Swaging Model. The finite-element model for the Microstructure Model was compiled from 4-noded tetrahedron elements. The resulting mesh and node numbers were 26,029 and 5,221 for Al powder/Fe, and 23,071 and 4,465 for Al–Mg–Si chip/Fe.

3.1.2 Description of Swaging Model

Figure 4 shows a perspective view of the Swaging Model and its mesh distribution. The work selected for analysis had diameters of 9.5 and 8 mm on the insertion and exit sides, respectively, assuming a taper with an angle of 3.5 degrees in
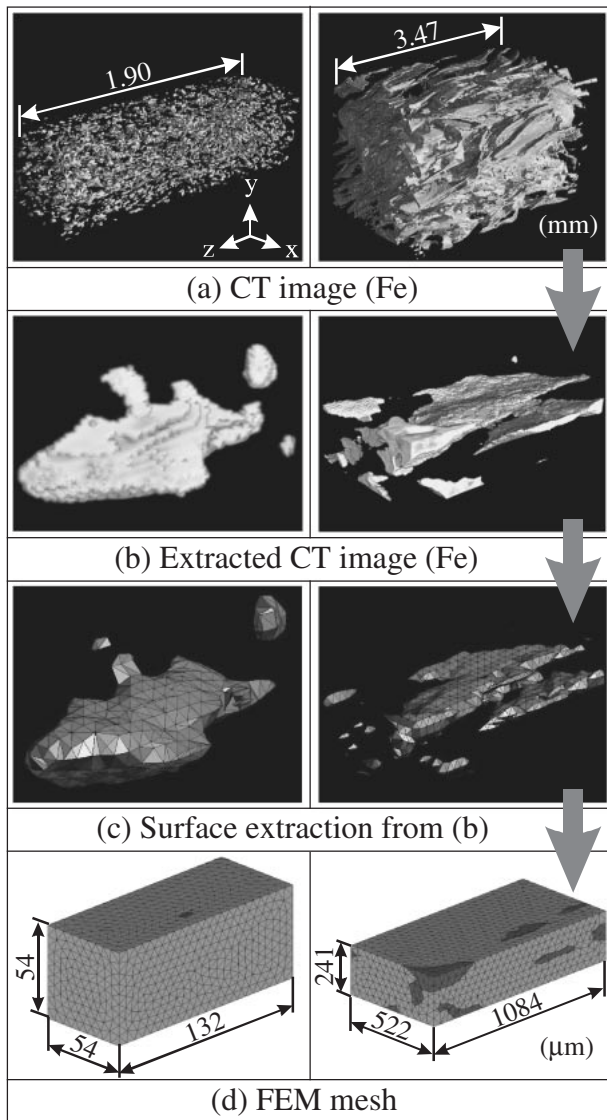

Fig. 3 Construction of finite element meshes from three-dimensional CT images. Small regions: (b) were extracted from the full CT volumes, and then surface extraction was performed for the meshing.
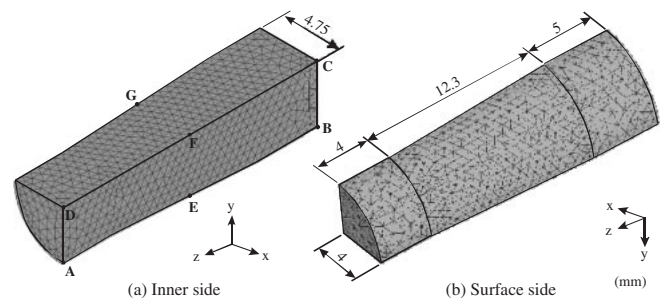

Fig. 4 Perspective views of three-dimensional finite element meshes shown from two directions. Homogenized mechanical properties were used for calculations. The small parallel-piped model (Microstructure model) is nested into this model (Swaging model).

between. The tapered segment was compressed by four dies during swaging. The material segments before and after the current swaging pass (5 and 4 mm in length, respectively) were attached to the tapered segment in order to take the constraints at both ends into account. The shape and dimensions were faithfully reproduced considering a single swaging pass at the applied strain of interest selected as described in section 2.2 (*i.e.* $\eta = 1.8$–2.1) and the swager actually used in the experiment as described in section 2.1.1. Owing to the axial symmetry of the Swaging Model and external forces, it was possible to represent the full work by modelling only a quarter of the work as shown in Fig. 4. The boundary conditions and the external displacement distribution are schematically illustrated in Fig. 5. The finite-element model for the Swaging Model was compiled from 10-noded tetrahedron elements. The mesh and node numbers were 10,385 and 16,024, respectively.

According to the principle of operation of a classical rotary swager, a motorized spindle is slotted in order to hold backers and the dies. The spindle passes the backers over rollers, so that each time the spindle passes over the backers one radial forming blow is executed, delivering a blow to the dies. This radial compression by the four dies pushes out the work, thereby squeezing it. The external displacement by the dies was assumed to be 61 μm according to the actual specifications of the swager used. The external displacement was applied incrementally to facilitate solution convergence. The local displacement distribution was calculated using the Swaging Model for use in the Microstructure Model as a set of boundary conditions.

3.2 Computation procedure

An elastic-plastic model with isotropic hardening was selected as representative of the behaviour of the two phases. Strain rate dependency was not taken into account. The materials were assumed to yield obeying an isotropic von Mises surface and later a Prandtl-Reuss associated flow rule. The materials were assumed to be completely solid throughout the deformation. For numerical simulation of the system of nonlinear equations, a Newton–Raphson iteration algorithm was implemented in which the applied displacement is increased stepwise up to the final value. The analysis was performed using the ANSYS software package with a DEC Alfa workstation.

Al/Fe composites deformed only up to $\eta = 1.8$ were not fully consolidated, so no valid stress–strain responses were available. Due to this lack of information on material properties for the Al/Fe composite at the applied strain of interest, the elastic modulus and elastic limit for the composite were estimated by the rule of mixture for use in the calculations for the Swaging Model. No strain hardening was assumed after yielding for the Al–Fe composites. In the case of the Microstructure Model, the input parameters for the properties of the aluminum matrix and the embedded iron phase were taken from experimental stress–strain curves for the monolithic materials. In order to obtain these data, first the microhardness values of the matrix and Fe phases were measured in the composite at the applied strain of interest (*i.e.* $\eta = 1.8$), then monolithic materials were swaged until the same microhardness values as for the composite were measured. The measured microhardness value of the Fe phase was HV127 and those for the matrices were HV55 and 123 for Al powder/Fe and Al–Mg–Si chip/Fe, respectively. These wires were then tensile-tested to obtain the input data. All of the input data are summarized in Fig. 6.

3.3 Calculated local stress distribution and its interpretation

Figure 7 shows contour maps of the equivalent plastic strain for the Swaging Model. The deformation of the materials within the tapered segment by the dies is con-
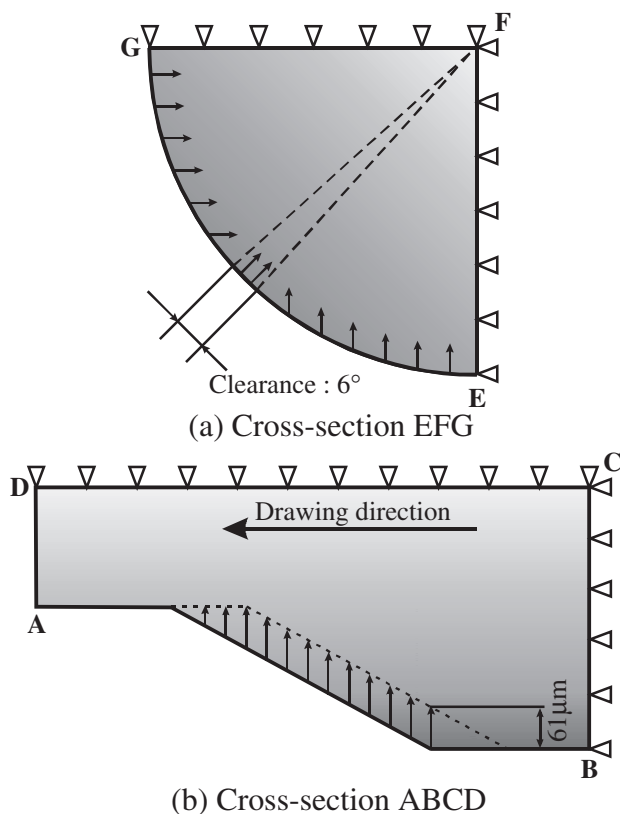

Fig. 5 Boundary conditions for swaging model shown in Fig. 3. EFG and ABCD cross-sections specified in Fig. 4 are shown here. Arrows indicate forced displacement of 61 mm by the movement of backers.
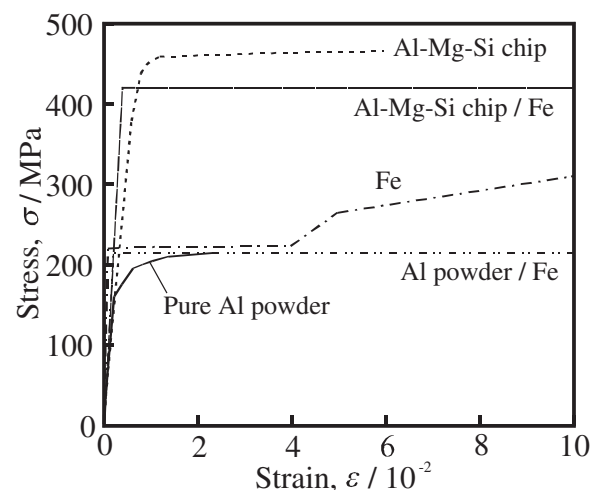

Fig. 6 True stress–true strain curves for consolidated monolithic aluminum and iron which were used as input data for Microstructure model. Those for Al–Fe composites used for Swaging model are also shown.
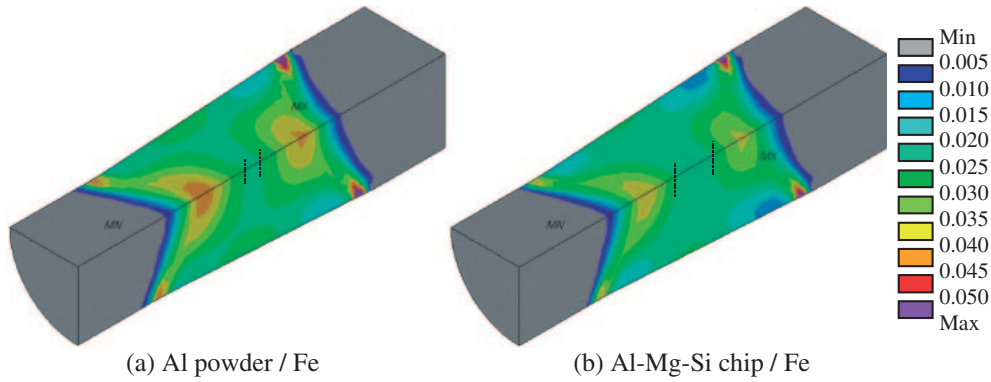
(a) Al powder / Fe (b) Al-Mg-Si chip / Fe

Fig. 7 Contour maps of equivalent plastic strain in Swaging models. Al powder/Fe and Al–Mg–Si chip/Fe composites are assumed. The dotted lines indicate the locations of Microstructure model.
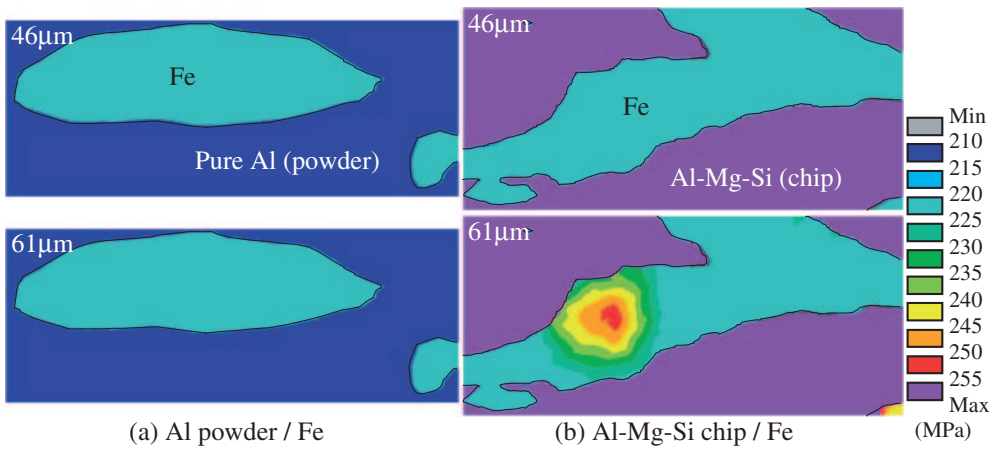

(a) Al powder / Fe (b) Al-Mg-Si chip / Fe (MPa)

Fig. 8 Contour maps of equivalent stress in Microstructure model. Applied displacements are 46 and 61 mm in the upper and lower maps, respectively.

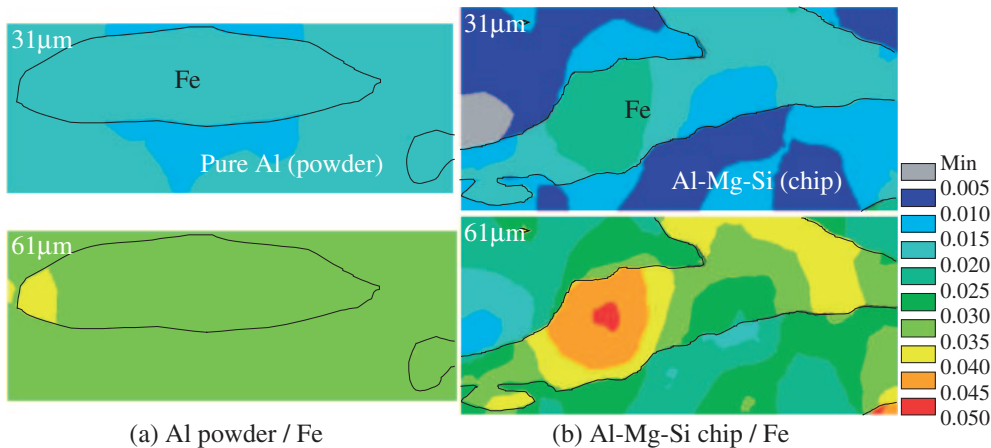(a) Al powder / Fe (b) Al-Mg-Si chip / Fe

Fig. 9 Contour maps of equivalent plastic strain in Microstructure model. Applied displacements are 31 and 61 mm in the upper and lower maps, respectively.

strained by neighbouring materials without forced displacement. Therefore, the maxima of equivalent strain are located adjacent to the insertion and output exits of the swager. However, strain distribution at the centre regions, where the Microstructure Model is located, appears to be relatively uniform. This implies that the location of the Microstructure Model does not greatly affect the computation results.

Figure 8 shows contour maps of the equivalent stress for the Microstructure Model at an intermediate and the final applied displacement levels. In Al powder/Fe, the stress distributions within the matrix and the Fe phase are almost uniform. The stress value within the Fe phase is not greatly in excess of its yield strength. On the other hand, in the case of Al–Mg–Si chip/Fe, although the stress distribution is also uniform at about 75% of the final displacement value, significant stress elevation is observed later at the final
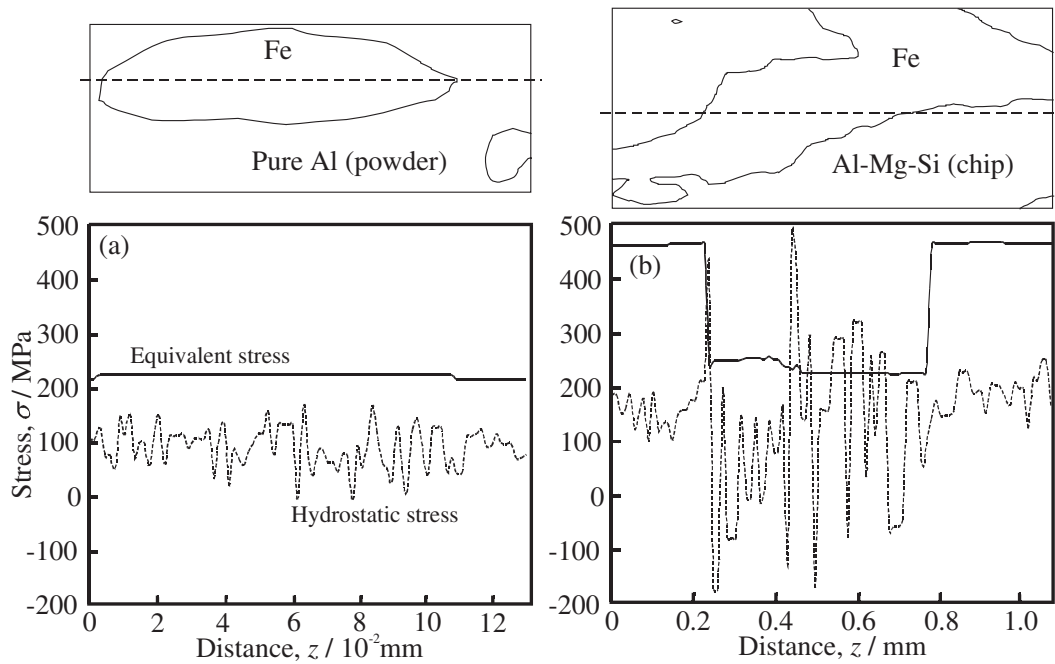
Fig. 10   Variations of equivalent stress and hydrostatic stress in Microstructure model.
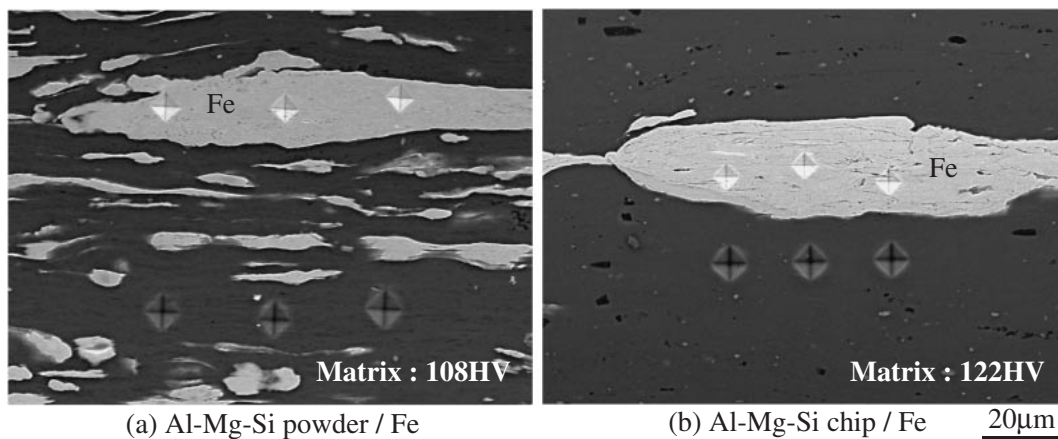

(a) Al-Mg-Si powder / Fe   (b) Al-Mg-Si chip / Fe   20μm

Fig. 11   SEM micrographs of longitudinal cross-sections of Al–20 vol%Fe composites swaged up to drawing strain of 5.4. Al–Mg–Si powder and chip were used as matrices in (a) and (b), respectively. The Al–Mg–Si powder was milled by a vibration ball milling apparatus for 14.4 ks before being mixed with Fe powder.

displacement level. The stress elevation is limited to a local region where the Fe phase is constricted or gnarled with flections. Figure 9 shows the corresponding equivalent plastic strain distributions. The contour map in Fig. 9(b) reveals inhomogeneous strain distribution corresponding to the stress distribution in the Fe phase. The tendency observed in Figs. 8 and 9 is consistent overall with the reported experimental results that the Fe phase can deform considerably only if aluminum cutting chip is used for the matrix. The equivalent strain distributions between the matrix and the Fe phase are similar in Al powder/Fe, while the maximum value of the Fe phase reaches more than double that of the matrix in Al–Mg–Si chip/Fe. However, considering that the yield point elongation of the Fe phase is about 0.04 as shown in Fig. 6, straining of the Fe phase is found to occur to some extent even in Al powder/Fe but falls marginally within the range of the yield point elongation

where an increase in the plastic strain occurs without an increase in the equivalent stress. It can therefore be inferred that the total processing conditions for Al powder/Fe fall one step short of the conditions necessary for multifilamentary microstructure formation.

Figure 10 shows the variations of equivalent stress and hydrostatic stress along the lines indicated in the figuer. In addition to the local elevation of equivalent stress, hydrostatic stress varies significantly in the Fe phase in Al–Mg–Si chip/Fe. It is well known that the plasticity of a material is increased by deformation under high hydrostatic pressure.[20] Elongation of the Fe phase may be promoted locally where the hydrostatic stress is high, and neighbouring regions may then be infectiously extended in the Fe phase.

Since stress elevation well beyond the yield strength of the Fe phase was predicted immediately before the applied displacement reached the final value, both the strengthening

of aluminum due to heavy deformation during cutting and irregular distribution of the Fe phase due to the shape of the cutting chip may be identified as essential factors for multifilamentary microstructure formation. As was introduced earlier in Table 1, in the series of trial productions of the Al/Fe composites, the matrix hardness was varied by the ball milling of an Al–Mg–Si alloy for various lengths of time. No significant elongation of the Fe phase was observed in this case even when the milling time was as long as 8 h. The microhardness value of the Al–Mg–Si aluminum matrix is shown in Fig. 11, with that of Al–Mg–Si chip/Fe is also shown in (b) for comparison. Although severe plastic deformation was applied to a similar alloy system with an identical temper condition (*i.e.* T6), the matrix hardness was obviously lower in the case of the milled powder than in the case of the cutting chip. This may be attributable to insufficient tempering of the original aluminum powder. Presumed causes for this may be the evaporation of magnesium during spraying of the aluminum melt and/or shortage or lack of an aging treatment for the powder.

Another factor may be responsible for the difference shown in Fig. 11. In a recent paper, the authors have reported that the consolidation of cutting chips by metalworking may be identified as an effective severe plastic deformation process involving two different severe deformation processes; namely, cutting and metalworking. The plastic strain introduced to a cutting chip during cutting was estimated to be 2.7–2.8 by geometrical consideration.[10] TEM observation revealed that much smaller grain size was obtained when the cutting chip was consolidated and swaged than when the same alloy was simply swaged to the same total strain levels.[10] This is analogous to metalworking by equal-channel angular pressing (ECAP).[21] In the case of repetitive pressing in ECAP, different microstructures are developed by rotating samples between consecutive passes. This is attributed to the change in slip systems activated on each consecutive pressing. It has been reported that there is no change in grain configuration and the microstructure consists essentially of subgrains separated by boundaries having low angles of misorientation when the rotation of a sample between consecutive pressings is 0 degree (*i.e.* activating identical slip systems).[21] Overall, it can be inferred that applying two different modes of shear deformation (*i.e.* cutting and swaging) might be clearly advantageous even if the large plastic strain accumulated during cutting (2.7–2.8) is not taken into account.

4.　Summary

In the present study, state-of-the-art techniques were applied to gain basic insight into essential factors for the microstructural development of Al–Fe composites. The approach taken in this study may be characterized as a new type of reverse engineering that is based on visualization of the microstructural features of materials.

It was clarified that local stress elevation occurs with inhomogeneous strain distribution where the Fe phase has an irregular shape when coarse cutting chips are used as a matrix. The significant variation of hydrostatic stress suggests that elongation of the Fe phase may be promoted locally

where the hydrostatic stress is high, and neighbouring regions may then be infectiously extended in the Fe phase. The tendency observed in the computation results was consistent overall with the reported experimental results that the Fe phase can deform considerably only if aluminum cutting chip is used for the matrix. It can be inferred that the processing conditions for Al–Fe composites reported in the literature fall one step short of the conditions necessary for multifilamentary microstructure formation. Both sufficient strengthening of the raw aluminum powder and effective strain accumulation were identified as being essential for multifilamentary microstructure formation. One possible procedure for the latter might be the application of two different modes of shear deformation, as was carried out for consolidation of the cutting chip (*i.e.* shear deformation during cutting and subsequent swaging).

REFERENCES

1) W. A. Spitzig and P. D. Krotz: Acta Metall. **35** (1987) 2427–2442.
2) G. Langford: Metall. Trans. **8A** (1977) 861–875.
3) C. L. H. Thieme, S. Pourrahimi and S. Foner: Scr. Metall. **28** (1993) 913–918.
4) T. Kobayashi and H. Toda: Mater. Sci. Forum **331–337** (2000) 1133–1138.
5) H. Toda and T. Kobayashi: *Special Issue, Int. J. of Mater. Product Tech.*, **SPM1** (2001) 427–432.
6) H. Mizutani, H. Toda and T. Kobayashi: Unpublished work (H. Mizutani, Master thesis, Toyohashi University of Technology) (2003).
7) Y. C. Lu, H. Kung, A. J. Griffin, M. Nastasi and T. E. Mitchell: J. Mater. Res. **12** (1997) 1939–1941.
8) Y. T. Chou: Can. J. Phys. **45** (1967) 559–566.
9) W. A. Spitzig and P. D. Krotz: Acta Metall. **36** (1988) 1709–1715.
10) Y. Fujii, H. Toda and T. Kobayashi: J. Jpn. Inst. Light Metal **53** (2003) 368–372 (in Japanese).
11) H. Toda, T. Kobayashi and J. Sawamura: *Proc. ICAA-9*, (2004) 1328–1333.
12) P. Cloetens, M. Pateyron-Salome, J. Y. Buffière, J. Peix, G. Baruchel, F. Peyrin and M. Schlenker: J. Appl. Phys. **81** (1997) 5878–5886.
13) E. Maire, L. Babout, J.-Y. Buffiere and R. Fougeres: Mater. Sci. Eng. A **319–321** (2001) 216–219.
14) G. Geandier, S. Denis, A. Mocellin, A. Hazotte and E. Maire: Scr. Mater. **48** (2003) 1219–1224.
15) D. Ulrich, B. Van Rietbergen, P. Rueegsegger and H. Weinans: J. Biomech. **31** (1998) 1187–1192.
16) N. Nakamori, T. Sudou, H. Kanamori, M. Endo and M. Kusakabe: *SPIE Proceedings 2708* (Physics of Medical Imaging) (1996), 696–705.
17) L. A. Feldkamp, L. C. Davis and J. W. Kress: J. Opt. Soc. Am. **1** (1984) 612–619.
18) H. Toda, I. Sinclair, J.-Y. Buffière, E. Maire, T. Connolley, M. Joyce, K. H. Khor and P. Gregson: Philos. Mag. A **83** (2003) 2429–2448.
19) H. Toda, I. Sinclair, J.-Y. Buffière, E. Maire, K. H. Khor, P. Gregson and T. Kobayashi: Acta Mater. **52** (2004) 1305–1317.
20) B. Dodd and Y. Bai: *Ductile Fracture and Ductility, Applications to Metalworking*, (London, Academic press 1987) p. 235.
21) T. G. Landon, M. Furukawa, M. Nemoto and Z. Horita: JOM **53** (2000) 30–33.